ACS MATERIALS LETTERS

www.acsmaterialsletters.org
Letter

Orbital-Engineered Amorphous 4d Chloride Cathodes Enabling High-Voltage, Multi-Electron, Electrolyte-Free Solid-State Batteries

Naoto Tanibata,* Shin Aizu, Takuhiro Sasadaira, Hayami Takeda, Masanobu Nakayama, and Koji Ohara

Cite This: https://doi.org/10.1021/acsmaterialslett.6c00297

ABSTRACT: Achieving high energy density in all-solid-state batteries is often hindered by sluggish ion transport and cathode anion instability. To address this challenge, we introduce a rational design strategy that exploits the strong d−p orbital hybridization inherent in amorphous 4d transition-metal chlorides. As a model system, amorphous $LiRuCl_4$ exhibits an exceptionally high room-temperature Li^+ diffusion coefficient of 4.8×10^{-9} cm^2 s^{-1}. When employed as an electrolyte-free cathode in an all-solid-state lithium-ion battery, it delivers an energy density of ∼472 Wh kg^{-1} (based on the total cathode mass) at 30 °C. Orbital-level stabilization of the M−Cl framework effectively suppresses Cl_2 evolution at potentials up to 4.4 V (vs. Li/Li^+), unlocking high-voltage multielectron chemistry. Consequently, this enhanced stability facilitates a highly reversible two-electron $Ru^{2+/3+/4+}$ redox process. Ultimately, engineering d−p hybridization in late transition-metal chlorides emerges as a promising design principle for developing next-generation high-energy-density solid-state battery cathodes.

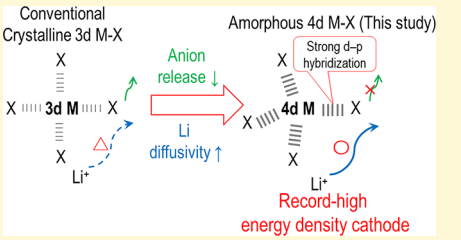

To address pressing energy and environmental challenges, the performance requirements for rechargeable batteries have become increasingly demanding in recent years.[1] Among emerging technologies, all-solid-state lithium-ion batteries have attracted considerable attention as promising next-generation systems because they are expected to simultaneously deliver high safety, high power capability, and high energy density.[2−4] In these systems, replacing flammable liquid electrolytes with solid electrolytes significantly reduces the risks of leakage and combustion.[5,6] Furthermore, the solid-state configuration enables the use of electrode materials that are unstable in liquid electrolytes due to dissolution, such as elemental sulfur[7,8] and metal chlorides,[9−11] thereby providing further opportunities to enhance energy density.

Chloride cathodes generally exhibit higher operating voltages than conventional oxide or sulfide counterparts owing to the high electronegativity of chlorine.[12] For the $Fe^{2+/3+}$ redox couple, the operating voltage of chloride Li_2FeCl_4 (3.6 V vs. Li/Li^+)[13] is higher than that of oxide Fe_2O_3 (∼1.5 V)[14] and sulfide Li_2FeS_2 (∼2.0 V),[15] and approaching $LiFePO_4$ (3.4 V), where the high voltage arises from the inductive effect of the PO_4 polyanion.[16] In conventional bulk-type all-solid-state batteries, solid electrolytes are incorporated into composite cathodes to provide ionic conduction pathways; however, such inactive components inevitably decrease the theoretical energy density at the electrode level.[17] Owing to the high polarizability of Cl^- and its relatively weak Coulombic interaction with Li^+, chlorides typically exhibit high Li diffusivity and mechanical deformability, and operation without added solid electrolyte has been demonstrated.[9] Nevertheless, previously reported chloride cathodes have been largely confined to crystalline materials employing 3d transition metals as redox centers,[9,13,18] thereby limiting the compositional and structural design space. Moreover, chlorine evolution at voltages above 4 V vs. Li/Li^+ poses a critical challenge, further hindering the realization of higher energy density.[19]

Meanwhile, Ishiguro and co-workers recently reported an amorphous chloride, $LiTaCl_6$, exhibiting exceptionally high Li-ion conductivity at room temperature ($\sigma = 1.0 \times 10^{-2}$ S cm^{-1}).[20] In general, compounds containing highly electronegative chlorine exhibit predominantly ionic bonding, and amorphous chlorides have rarely been reported.[21] $LiTaCl_6$ is considered to adopt an amorphous structure because the relatively strong covalency between high-valent Ta^{5+} (a 5d transition metal) and Cl^- suppresses the formation of long-range order.[22] In recent years, amorphous chloride materials have emerged as promising solid electrolytes owing to their high ionic conductivity and structural flexibility.[23] In this study, we aim to realize similarly high Li diffusivity in cathode materials. Previously reported 3d transition-metal chlorides have been synthesized by mechanical milling; however, unlike more covalent sulfides, they do not readily form amorphous phases and instead remain crystalline because of the predominantly ionic character of the M−Cl bonds.[24,25] We therefore hypothesized that increasing M−Cl covalency would promote amorphization and accordingly focused on chlorides incorporating 4d transition metals as redox centers. Late transition metals possess more spatially extended d orbitals, leading to increased covalency with counter anions.[22] Such enhanced covalency is also expected to stabilize chlorine and suppress its evolution at high voltages.

However, Li−Cl compounds incorporating 4d transition metals are scarcely represented in existing materials databases. For example, only three entries (mp-28463: $LiNb_3Cl_8$; mp-29985: $LiNb_6Cl_{19}$; mp-686087: $Li_3(Nb_2Cl_5)_8$) are currently listed in the Materials Project database.[26] These compounds contain low-valent Nb species (Nb^{2+}/Nb^{3+}) and have low Li content, rendering them unsuitable for high-

Received: March 24, 2026
Revised: June 1, 2026
Accepted: June 4, 2026

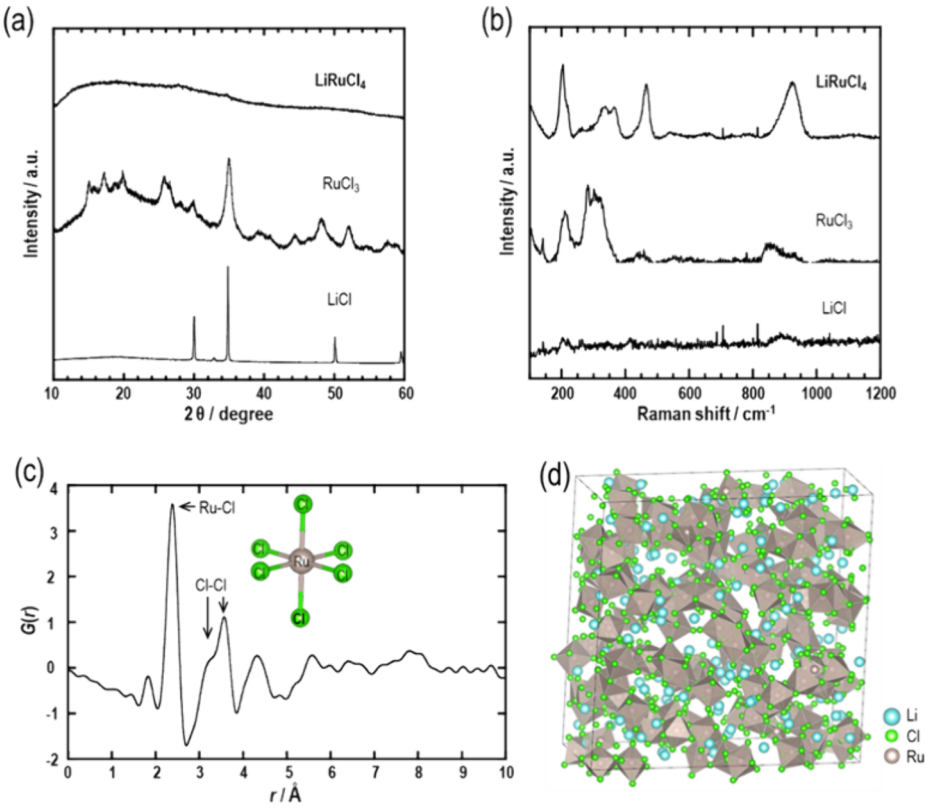

Figure 1. Structural characterization of $LiRuCl_4$ synthesized via a mechanochemical method. (a) X-ray diffraction (XRD) patterns and (b) Raman spectra of synthesized $LiRuCl_4$ and the starting materials ($RuCl_3$ and LiCl). (c) Radial distribution function (RDF) obtained from total scattering measurements of the $LiRuCl_4$. The sample density estimated from baseline fitting during the RDF analysis was approximately 2.98 g cm^{-3}. (d) Three-dimensional structure of amorphous $LiRuCl_4$ obtained from RMC analysis.

voltage cathode applications. To overcome this limitation, we employed a machine-learning-based, composition-driven synthesizability prediction framework to evaluate synthetic accessibility from composition (see Table S1 and Supplementary Note 1 for details).[27] We selected 4d transition metals that exhibit multiple accessible oxidation states while excluding the radioactive element Tc. Accordingly, Nb, Mo, Ru, and Pd were selected as candidate redox centers. Next, considering cathode materials that operate from a charged state, we assumed that the initial composition should contain relatively low-valent metal ions. Accordingly, Li compounds incorporating low-valent 4d transition-metal ions (M^{2+} or M^{3+}; M = Nb, Mo, Ru, Pd) were selected as screening targets. Specifically, compositions represented by $Li_xM^{2+}Cl_{x+3}$ and $Li_xM^{3+}Cl_{x+2}$ (x = 1–3) were evaluated using the machine-learning approach[27] to estimate their synthetic accessibility (see Table S1). Among the candidates predicted to have relatively high synthetic feasibility, we focused on $LiRuCl_4$, which contains Ru, a 4d transition metal with a well-established track record as a redox center in oxide cathode materials for lithium-ion batteries.[28−30] We therefore investigated its structure and electrochemical properties as a chloride cathode material. We demonstrate that strong d−p orbital hybridization in transition-metal chlorides drives amorphization, enhances lithium diffusivity, and suppresses anion release, thereby enabling high-energy-density, electrolyte-free cathodes to operate at elevated voltages and access multi-electron redox regimes.

$LiRuCl_4$ was synthesized via a mechanochemical method, which is known to facilitate amorphization.[31] The X-ray diffraction (XRD) pattern of the obtained black powder (Figure 1a) showed no discernible crystalline peaks, including those of the starting materials, but instead exhibited a broad halo, indicating the formation of an amorphous phase. The Raman spectrum of the synthesized sample showed no peaks attributable to the starting materials (LiCl and $RuCl_3$), suggesting the formation of an amorphous $LiRuCl_4$ phase with a distinct bonding environment (Figure 1b). To elucidate the local structure of amorphous $LiRuCl_4$, total scattering measurements were performed (Figure 1c). The peaks in the corresponding radial distribution function (RDF) were compared with reported interatomic distances for representative Ru−Cl compounds (Figure S1a−c: $Rb_2LiRuCl_6$ and $RuCl_3$ with face-sharing octahedra; and $RuCl_3$ with edge-sharing octahedra; see Table S2). The most intense peak in the RDF of $LiRuCl_4$ (Figure 1c), located at approximately 2.40 Å, corresponds closely to the nearest-neighbor Ru−Cl distances (2.35−2.39 Å) in the compounds containing $RuCl_6$ octahedra. In addition, peaks at approximately 3.20 and 3.75 Å correspond to the nearest Cl−Cl distances (3.21−3.36 Å) and second-nearest Cl−Cl distances (3.75−4.39 Å), respectively, in these $RuCl_6$-based compounds. These results indicate that the obtained material is an amorphous $LiRuCl_4$ phase composed of $RuCl_6$ octahedral units as the fundamental structural motif. One plausible origin of the amorphization of $LiRuCl_4$, despite its sharing MCl_6 octahedral units common to 3d transition-metal chlorides, is the enhanced covalency of the M−Cl bonds arising from the more spatially extended 4d orbitals, which likely suppresses the formation of long-range order required for crystallization.

To gain further structural insights into amorphous $LiRuCl_4$, we analyzed its three-dimensional structure using reverse Monte Carlo (RMC) modeling based on X-ray total scattering data (Figures 1d and S2). As shown in Figure S2a, the structural model obtained by the RMC method (Figure 1d) reproduces the experimental total scattering data $S(Q)$ well. Quantification of the coordination numbers from this structural model confirmed, as mentioned earlier, that Ru is primarily organized into $RuCl_6$ octahedra (CN = 6) (73.2%,

https://doi.org/10.1021/acsmaterialslett.6c00297
ACS Mater. Lett. XXXX, XXX, XXX–XXX

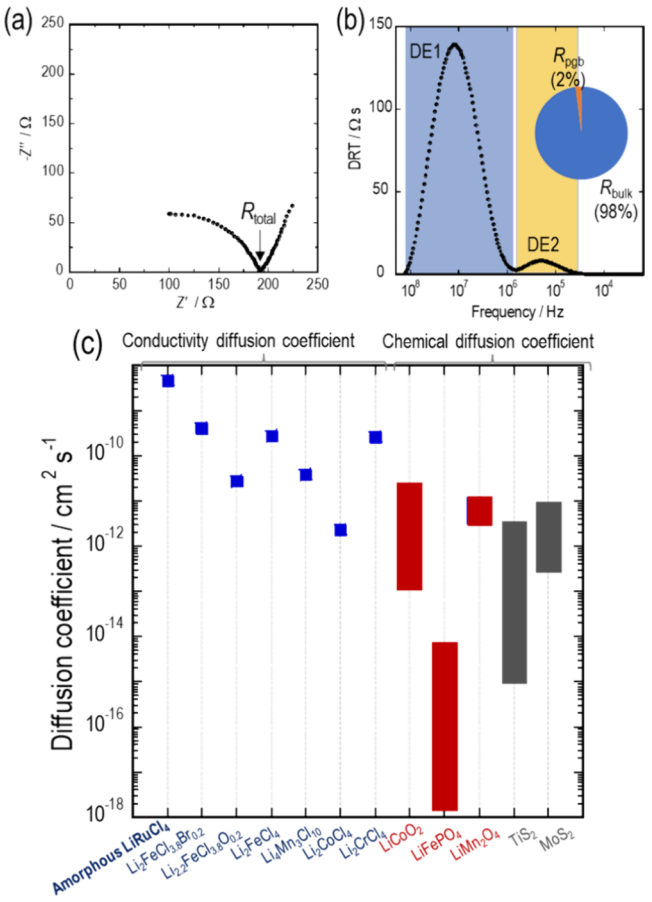

Figure 2. Li-ion diffusivity of an amorphous $LiRuCl_4$ pellet. (a) Nyquist plot of the pellet; the Li-ion conductivity was calculated from the total resistance (R_{total}). (b) Distribution of relaxation time (DRT) spectrum. The inset pie chart shows the relative contributions of the bulk resistance (R_{bulk}) and particle grain-boundary resistance (R_{pgb}). (c) Comparison of the conductivity diffusion coefficients of transition-metal chloride cathodes, including amorphous $LiRuCl_4$, with reported chemical diffusion coefficients of representative oxide and sulfide cathodes. Representative oxide cathodes: $LiCoO_2$, $LiFePO_4$,[32] $LiMnO_2$.[33] Representative sulfide cathodes: TiS_2,[34] MoS_2.[35] Other transition-metal chloride cathodes: Li_2FeCl_4,[13] $Li_2FeCl_{3.8}Br_{0.2}$,[36] $Li_{2.2}FeCl_{3.8}O_{0.2}$,[19] $Li_4Mn_3Cl_{10}$,[24] Li_2CoCl_4, Li_2CrCl_4.[25]

Figure S2b). As shown in Figure S2c, these polyhedra are connected via a variety of bonding modes (isolated, vertex, edge, and face sharing) characteristic of amorphous structures. On the other hand, the distribution of Ru coordination numbers around Cl shown in Figure S2d reveals that Cl exists primarily as terminal Cl (CN = 1, 58.6%) and bridging Cl (CN = 2, 38.2%). It was also found that only a very small amount (1.8%) of Cl is not coordinated to Ru. This structural feature, wherein "almost all Cl is coordinated to Ru," is considered to be one of the factors suppressing Cl release in this material, as will be shown later.

The Nyquist plot obtained from AC impedance measurements is shown in Figure 2a. The ionic conductivity of the pellet, calculated from the total resistance (R_{total}), was 2.5×10^{-4} S cm^{-1}, more than two orders of magnitude higher than the electronic conductivity measured by DC polarization (4.0×10^{-6} S cm^{-1}; Figure S3). These results confirm that Li^+ ions are the dominant charge carriers in this material. To quantitatively compare ionic transport with other transition-metal-based cathodes, the conductivity was converted to a conductivity diffusion coefficient (4.8×10^{-9} cm^2 s^{-1}) using the Nernst–Einstein equation. Figure 2c compares this value with reported chemical diffusion coefficients of representative oxide cathodes ($LiCoO_2$, $LiFePO_4$,[32] $LiMnO_2$[33]) and sulfide cathodes (TiS_2,[34] MoS_2[35]), as well as conductivity diffusion coefficients of other transition-metal chloride cathodes (Li_2FeCl_4,[13] $Li_2FeCl_{3.8}Br_{0.2}$,[36] $Li_{2.2}FeCl_{3.8}O_{0.2}$,[19] $Li_4Mn_3Cl_{10}$,[24] Li_2CoCl_4, Li_2CrCl_4[25]). The calculated conductivity diffusion coefficient assumes a thermodynamic factor of unity and thus generally underestimates the true chemical diffusion coefficient.[37,38] Nevertheless, chloride materials exhibit conductivity diffusion coefficients that are comparable to or higher than the chemical diffusion coefficients of representative oxide and sulfide cathodes. Notably, amorphous $LiRuCl_4$ displays one of the highest Li diffusion coefficients among these materials, strongly supporting the potential of amorphous chloride cathodes. This high Li^+ diffusivity is consistent with the fast Li transport previously reported for amorphous chlorides such as $LiTaCl_6$.[20]

To further deconvolute the resistance contributions, distribution of relaxation time (DRT) analysis was conducted (Table S3). As shown in Figure 2b, two distinct resistance components (DE1 and DE2) were identified. The associated capacitance (C) was calculated from the fitted relaxation time (DE–T) and resistance (DE–R) using C = DE–T/DE–R.[39] The capacitance of DE1 (5.5×10^{-11} F) is on the same order of magnitude as the bulk capacitance estimated from typical solid-state dielectric constants (~10^{-12} F),[40] indicating that DE1 corresponds to the bulk resistance. Based on the particle size (~3 μm) observed in SEM images (Figure S4a), the particle grain-boundary capacitance estimated using the brickwork model[25,40] (~3×10^{-8} F) agrees well with that of DE2 (1.6×10^{-8} F), suggesting that DE2 primarily originates from particle grain boundaries. Importantly, this grain-boundary resistance accounts for only ~2% of the total resistance. The low particle-grain-boundary resistance, likely arising from the high deformability of amorphous $LiRuCl_4$ particles, contributes to the high Li diffusivity of the pellet. SEM images of the fractured pellet surface (Figure S4b) reveal dense particle packing, confirming the high deformability of $LiRuCl_4$. Moreover, DRT analysis identified only bulk and particle grain-boundary contributions, with no detectable crystallite-grain-boundary component typically observed in crystalline materials,[22] further supporting the intrinsically fast Li transport in amorphous $LiRuCl_4$.

To further investigate the Li diffusion mechanism quantitatively, we performed temperature-dependent AC impedance measurements and evaluated the activation energy and pre-exponential factor based on the Arrhenius plot (Figure S5). The results showed that the material exhibited good Arrhenius behavior, with an activation energy of 0.40 eV and a pre-exponential factor of 2.3×10^5 K S cm^{-1}. When compared to Li_2FeCl_4, a crystalline material of the same chloride system (diffusion coefficient: 1.9×10^{-10} cm^2 s^{-1}, activation energy: 0.40 eV, pre-exponential factor: 3.5×10^4 K S cm^{-1}),[13] it is evident that while the activation energy of the present material is comparable, the pre-exponential factor of amorphous $LiRuCl_4$ is one order of magnitude larger, resulting in a proportionally higher diffusion coefficient. This increase in the pre-exponential factor may be attributed to the site diversity and increased number of continuous conduction paths characteristic of amorphous structures.

An all-solid-state lithium-ion battery was assembled with an electrolyte-free cathode comprising amorphous $LiRuCl_4$ as the active material, and its galvanostatic charge–discharge performance was evaluated. As shown in Figure 3a, the cell operated stably at room temperature (30 °C). This reversible operation without electrolyte additives is attributed to the intrinsically high Li diffusivity of amorphous $LiRuCl_4$. In previously reported chloride cathodes based on 3d transition metals, chlorine evolution at ~4.0 V vs. Li/Li^+ has posed a critical limitation.[19] In contrast, $LiRuCl_4$ operates reversibly at a higher voltage of 4.4 V vs. Li/Li^+. This enhanced high-voltage stability is attributed to stronger hybridization between metal 4d and Cl 3p orbitals compared with 3d systems,[41,42] which stabilizes M–Cl bonds and suppresses Cl_2 evolution at elevated potentials. These results indicate that chloride instability above 4 V is not intrinsic to chloride cathodes but instead arises from insufficient metal–ligand orbital overlap in 3d-based systems.

https://doi.org/10.1021/acsmaterialslett.6c00297
ACS Mater. Lett. XXXX, XXX, XXX–XXX

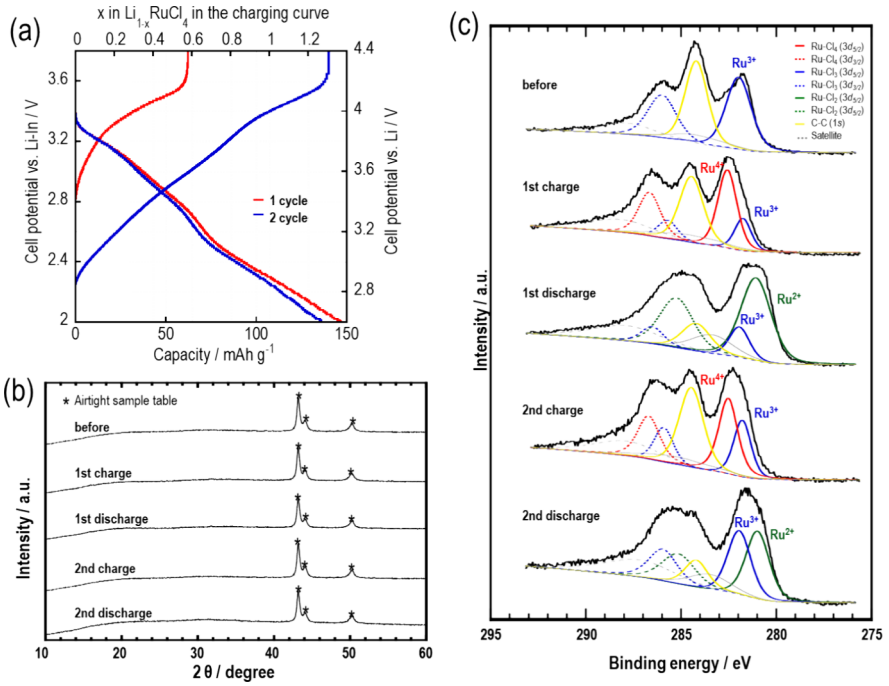

Figure 3. Charge−discharge behavior of amorphous $LiRuCl_4$. (a) Galvanostatic charge−discharge curves of an all-solid-state lithium-ion battery employing a composite cathode consisting of amorphous $LiRuCl_4$ as the active material and Ketjen Black (KB) as the conductive additive. The first and second cycles are shown in red and blue, respectively. (b) XRD patterns and (c) Ru 3d XPS spectra of the composite cathode (amorphous $LiRuCl_4$ + KB) at different states during charge and discharge.

Furthermore, the cell delivered a reversible capacity of ∼150 mAh g^{-1}, exceeding the theoretical one-electron capacity of $LiRuCl_4$ (107 mAh g^{-1}). This observation suggests that multi-electron redox processes occur reversibly within the investigated voltage window.

To elucidate the charge−discharge mechanism of amorphous $LiRuCl_4$, XRD and XPS measurements were performed on the cathode composite at five distinct states of charge. None of the five XRD patterns (Figure 3b) exhibited discernible crystalline peaks, confirming that the material remains amorphous throughout cycling. In the Ru 3d XPS spectra (Figure 3c), a single peak primarily assigned to Ru^{3+} was observed before cycling, whereas charging introduced a new high-binding-energy component attributable to Ru^{4+} and discharging generated a low-binding-energy component attributable to Ru^{2+}. To quantitatively demonstrate this multi-electron mechanism, we deconvoluted the oxidation state of Ru based on XPS peak areas and compared it with the theoretical charge compensation derived from the electrochemical capacity (Figure S6). The ratios derived from the XPS spectra of Ru^{2+}, Ru^{3+}, and Ru^{4+} under various charge-discharge states are in good agreement with the trends of the predicted values calculated from the specific capacity. These observations conclusively demonstrate that a highly reversible two-electron redox process involving $Ru^{2+/3+/4+}$ proceeds in the voltage range of 2.6−4.4 V (Li/Li^+ pair). The same two-electron behavior was reproduced in the second cycle, demonstrating the reversibility of the multi-electron redox process. Moreover, the Cl/Ru ratio derived from XPS quantification (Table S4) remained ≈4 (molar) before and after cycling, consistent with the nominal composition and suggesting substantially suppressed Cl_2 loss even at 4.4 V (vs. Li/Li^+), although trace-level Cl_2 evolution cannot be completely excluded without direct gas analysis. Taken together, these results indicate that the 4d transition metal Ru stabilizes chlorine through enhanced metal−ligand interactions, thereby suppressing Cl_2 evolution and enabling reversible multi-electron redox in this chloride cathode.

To quantitatively assess the enhancement of d−p orbital hybridization upon substitution of 3d with 4d transition metals, we performed Crystal Orbital Hamilton Population (COHP) analysis[43] based on spin-polarized DFT calculations using crystalline model structures, given that direct first-principles calculations of the amorphous structure (1008 atoms for RMC calculations) are computationally intractable (Figure S7). Specifically, we constructed two crystalline models sharing the same MCl_6 octahedral framework: the metastable delithiated spinel chloride $LiFeCl_4$ reported in our previous paper[19] and a $LiRuCl_4$ model derived by substituting Fe with Ru in the same structure followed by full structural relaxation. COHP analysis was subsequently applied to the converged wavefunctions. The integrated COHP values (−ICOHP) averaged over all nearest-neighbor M−Cl bonds up to the Fermi level were 1.78 eV per bond for Fe−Cl and 2.66 eV per bond for Ru−Cl, indicating that the covalency of Ru−Cl bonds is approximately 49% greater than that of Fe−Cl bonds. This result is consistent with the enhanced d−p hybridization arising from the more spatially extended Ru 4d orbitals relative to Fe 3d, and provides direct theoretical support for the substantial strengthening of M−Cl covalency upon introduction of a 4d transition metal. Further computational details and results are provided in the Supporting Information.

The cathode-mass-based energy density, calculated from the initial discharge curve of amorphous $LiRuCl_4$, was approximately 472 Wh kg^{-1}. It is worth noting that this value is calculated based on the total weight of the cathode composite (active material and conductive additives, in a 90:10 weight ratio), rather than the active material alone. This provides a more rigorous basis for comparison with conventional composite cathodes that require a solid electrolyte. Table 1 compares this value with those of all-solid-state batteries employing representative oxide cathodes ($LiCoO_2$, $LiFePO_4$, $LiMn_2O_4$) and chloride cathodes (Li_2FeCl_4, Li_3TiCl_6, $LiVCl_3$). These comparisons demonstrate that the battery utilizing amorphous $LiRuCl_4$ as the active material outperforms conventional all-solid-state batteries in terms of energy density. This enhanced performance arises from the intrinsically high Li diffusivity of amorphous $LiRuCl_4$, which enables an electrolyte-free electrode configuration, as well as from high-voltage operation and reversible multi-electron redox enabled by strong d−p orbital hybridization.

https://doi.org/10.1021/acsmaterialslett.6c00297
ACS Mater. Lett. XXXX, XXX, XXX−XXX

Table 1. Comparison of the Energy Densities of All-Solid-State Batteries Employing $LiRuCl_4$ as the Active Material with Those Using Representative Oxide Cathodes ($LiCoO_2$, $LiFePO_4$, $LiMn_2O_4$) and Chloride Cathodes (Li_2FeCl_4, Li_3TiCl_6, $LiVCl_3$)[a,b]

	energy density per cathode weight (Wh kg^{-1})	cathode active material (CAM)	solid electrolyte (SE)	weight % in cathode (CAM/SE/others)	coating for CAM
this work	472	$LiRuCl_4$	Li_2ZrCl_6	90:0:10	none
Zhang et al. (2018)[46]	308	$LiCoO_2$	$Li_{10}GeP_2S_{12}$ with LiH_2PO_4 coating to Li	70:30:0	$LiNbO_3$
Auvergniot et al. (2017)[47]	239		Li_6PS_5Cl	38:57:5	none
Asano et al. (2018)[48]	380		Li_3YCl_6	82.4:17.6:0	none
Li et al. (2019)[49]	293		Li_3InCl_6	70:30:0	none
Park et al. (2020)[50]	308		$Li_{2.633}Er_{0.633}Zr_{0.367}Cl_6$	70:30:0	none
Liang et al. (2020)[51]	341		Li_3ScCl_6	70:30:0	none
Kwak et al. (2021)[52]	430		$Li_{2.25}Zr_{0.75}Fe_{0.25}Cl_6$	68:29:3	none
Wang et al. (2021)[53]	379		Li_2ZrCl_6	70:30:0	none
Kwak et al. (2023)[54]	491		ZrO_2-$2Li_2ZrCl_5F$	68:29:3	none
Sakuda et al. (2012)[16]	144	$LiFePO_4$	$80Li_2S$-$20P_2S_5$	38:38:4	carbon
Yan et al. (2016)[55]	113		$Li_7La_3Zr_2O_{12}$	24:56:20	carbon
Cronk et al. (2023)[56]	63		Li_6PS_5Cl	40:57:3	carbon
Cronk et al. (2023)[56]	184		Li_2ZrCl_6	40:57:3	carbon
Kitaura et al. (2011)[57]	111	$LiMn_2O_4$	$80Li_2S$-$20P_2S_5$	38.5:57.7:3.8	$Li_4Ti_5O_{12}$
Kitaura et al. (2011)[57]	81		$80Li_2S$-$20P_2S_5$	38.5:57.7:3.8	none
Auvergniot et al. (2017)[47]	105		Li_6PS_5Cl	38:57:5	none
Tanibata et al. (2022)[11]	252	Li_2FeCl_4	$LiAlCl_4$	70:20:10	none
Wang et al. (2023)[9]	230	Li_3TiCl_6	catholyte: Li_2ZrCl_6, separator and anolyte: Li_6PS_5Cl	95:0:5	none
Liang et al. (2023)[18]	214	$LiVCl_3$	catholyte: Li_3InCl_6, separator and anolyte: Li_6PS_5Cl	45.5:45.5:9	none
Tanibata et al. (2025)[19]	330	$Li_{2.2}FeCl_{3.8}O_{0.2}$	Li_2ZrCl_6	90:0:10	none

[a]The table lists (from left to right) energy density, cathode active material (CAM), solid electrolyte (SE), cathode composition ratio (CAM/SE/others), and the presence or absence of CAM surface coating. [b]The comparison values are based on the data reported in the respective references.

Although the cathode-level energy density is high as described above, the practical stack-level energy density is inevitably reduced due to the presence of inert materials required for cell fabrication. To provide a realistic perspective, we estimated the stack-level energy density based on a hypothetical cell configuration[44] (Supplementary Note 2). Assuming a practical cathode loading of 15.0 mg cm^{-2}, a solid electrolyte separator (3.6 mg cm^{-2}), a lithium metal anode (1.07 mg cm^{-2}), and Cu/Al current collectors (8.96 and 2.7 mg cm^{-2}, respectively) (Table S5), the total areal density of the stack is 31.33 mg cm^{-2}. The stack-level energy density based on this configuration is estimated to be approximately 226 Wh kg^{-1}. Although this represents a decrease from cathode-based values (a challenge common to all current all-solid-state battery evaluations), this estimated stack-level energy density remains highly competitive and clearly demonstrates the practical advantages of the "electrolyte-free configuration" enabled by amorphous $LiRuCl_4$.

Furthermore, AC impedance measurements before and after cycling (Figure S8) reveal a negligible semicircular component typically associated with charge-transfer resistance. The low interfacial resistance is likely attributable to the favorable interface formed between the chloride cathode and chloride solid electrolyte,[11] together with the structural flexibility and configurational freedom inherent to amorphous materials.[22,45] In addition, the rate capability of $LiRuCl_4$ (Figure S9) remains robust, maintaining a capacity of 73 mAh g^{-1} at a current density of 0.064 mA cm^{-2} after cycles.

To directly demonstrate the practical advantages of the electrolyte-free design, we fabricated a composite cathode incorporating a conventional solid electrolyte and compared its rate characteristics with those of the electrolyte-free configuration. For the solid electrolyte, we used Li_2ZrCl_6, a chloride salt that was rationally selected not only for its high ionic conductivity but also for its ability to suppress degradation caused by acid–base reactions[11] at the electrode/electrolyte interface. Figure S10 shows a comparison of the rate characteristics between the electrolyte-free electrode and the electrolyte-added electrode. When comparing the discharge capacity per unit mass of active material (Figure S10a), the electrolyte-added electrode exhibited a slightly higher capacity at both low and high rates due to the formation of high-ion-conductivity pathways by the added electrolyte. However, when comparing the capacity per unit mass of the entire composite cathode (Figure S10b), the electrolyte-free electrode exhibited a significantly higher capacity at all current densities. These results demonstrate that the high Li diffusivity of amorphous $LiRuCl_4$ allows for the complete elimination of inert solid electrolyte components from the cathode, thereby maximizing practical capacity and energy density at the electrode level without significantly compromising reaction kinetics.

We introduce an amorphous chloride cathode concept centered on electronic-structure engineering via strong transition metal−chlorine d−p hybridization, aimed at enabling high-energy-density all-solid-state batteries. Targeting 4d transition metals with spatially extended d orbitals, we combined machine-learning−assisted synthesizability screening with mechanochemical synthesis to realize amorphous $LiRuCl_4$ composed of $RuCl_6$ octahedral units. The as-prepared material exhibits an exceptionally high Li diffusion coefficient of 4.8×10^{-9} cm^2 s^{-1} at room temperature in pressed (green) pellets, outperforming conventional cathodes. When employed as an electrolyte-free cathode in all-solid-state lithium batteries, it achieves an energy density of ≈472 Wh kg^{-1} (per cathode mass), exceeding previously reported systems. Crucially, chlorine evolution near ∼4 V (vs. Li/Li^+)—a common failure mode in 3d transition-metal chlorides—is effectively suppressed by strong d−p hybridization with the 4d metal center, enabling a reversible two-electron $Ru^{2+/3+/4+}$ redox process. These findings demonstrate that orbital-level electronic-structure tuning can concurrently stabilize the anion framework and activate high-

https://doi.org/10.1021/acsmaterialslett.6c00297
ACS Mater. Lett. XXXX, XXX, XXX−XXX

voltage multielectron redox chemistry. Collectively, this work demonstrates the potential of orbital engineering in late transition-metal chlorides as a promising strategy to extend electrolyte-free cathodes into higher-voltage and multielectron regimes. By shifting chloride cathode development from empirical discovery to rational, electronic-orbital–driven design, this work provides a conceptual framework for next-generation high-energy-density all-solid-state batteries.

■ EXPERIMENTAL SECTION

Synthesis of Amorphous $LiRuCl_4$

Amorphous $LiRuCl_4$ was synthesized by mechanochemical milling. LiCl (99.9%, Kishida Chemical Co., Ltd.) and $RuCl_3$ (99.99%, Thermo Fisher Scientific Co., Ltd.) were mixed in a stoichiometric ratio and loaded into a 45 mL ZrO_2 milling pot with 30 g of 5 mm ZrO_2 balls. Milling was carried out using a planetary ball mill (P-7 classic-line, Fritsch Japan K.K.) at 500 rpm for 15 min followed by a 10 min pause per cycle, for a total of 32 cycles.

Phase identification was performed by powder X-ray diffraction (XRD; MiniFlex 600, Rigaku Corp.) using Cu Kα radiation. X-ray total scattering measurements were conducted at BL04B2 beamline in SPring-8, Japan, to study the local structure by radial distribution function (RDF) analysis.[58] An incident X-ray energy of $E = 61.3$ keV was used with hybrid detectors of Ge and CdTe. We conducted structural refinement by using the RMC program (RMC_POT),[59] to determine the structural models, which reproduces the experimentally observed $S(Q)$. An initial structural model for RMC analysis was constructed based on a $LiCrF_4$ framework (mp-759949), which consists of MX_6 octahedra with the same composition type. In this model, Cr and F atoms were substituted with Ru and Cl, respectively, to generate a $LiRuCl_4$ configuration. A supercell containing 1159 atoms was then constructed. Molecular dynamics (MD) simulations were performed using pretrained universal neural network potential, preferred potential (ver.4.0.0) implemented in Matlantis software package[60] to obtain a realistic amorphous structure. The system was first equilibrated under NPT conditions at 873 K for 1 ns, followed by further equilibration at 273 K under NPT conditions for 1 ns. Subsequently, an NVT simulation at 273 K was conducted. The resulting structure was used as the initial configuration for the RMC analysis. Since the MD simulation results well reproduced the nearest neighbor polyhedron structures, we constrained the local structural parameters, including the nearest-neighbor Ru–Cl and Li–Cl distances and the Cl–Ru–Cl intrapolyhedron angles that define the local $RuCl_x$ geometry. Minimum cutoff distances of 1.95 Å for Ru–Cl, 1.50 Å for Li–Cl, 1.50 Å for Cl–Cl, 1.50 Å for Ru–Li, 1.50 Å for Li–Li, and 3.00 Å for Ru–Ru were applied to avoid unphysically short interatomic distances during refinement. Raman spectra were acquired with a Raman spectrometer (NRS-3300, JASCO Corp.) using a 633 nm excitation source.

Ionic Conductivity Measurements

Ionic conductivity was evaluated by AC impedance spectroscopy. Approximately 70 mg of powder was pressed between Au-coated stainless-steel electrodes at 382 MPa to form pellets (10 mm diameter, ∼0.50 mm thickness). Impedance measurements were performed at 25 °C using a VSP electrochemical workstation (BioLogic) with a 10 mV AC amplitude over a frequency range of $100–10^6$ Hz. DC polarization measurements were conducted under identical conditions by applying 5 mV for 25 min at 25 °C. Distribution of relaxation time (DRT) analysis[61] was carried out using Z-Assist software (TOYO Co.) to deconvolute bulk and interparticle resistances. The impedance spectra were subsequently fitted by complex nonlinear least-squares analysis with time constants fixed according to the DRT results. The cross-sectional morphology of pressed pellets was examined by scanning electron microscopy (SEM; JSM-6360LV, JEOL) to assess mechanical deformability.

All-Solid-State Battery Fabrication and Electrochemical Characterization

The cathode composite was prepared by mixing $LiRuCl_4$ and conductive carbon (Ketjenblack, Lion Corp.) at a weight ratio of 90:10. Li_2ZrCl_6 solid electrolyte was first pressed at 96 MPa to form a pellet. Approximately 5 mg of the cathode composite was spread onto the electrolyte pellet and co-pressed at 382 MPa. A Li–In alloy[62] served as the counter/reference electrode. Au-coated stainless-steel disks (10 mm diameter) were used as current collectors to assemble all-solid-state lithium cells.

Galvanostatic charge–discharge tests were conducted at 0.013 mA cm^{-2} within a voltage window of 2.62–4.42 V (vs. Li/Li^+). Rate capability was evaluated in the same voltage range by stepwise varying the current density (0.0064, 0.013, 0.025, 0.038, and 0.064 mA cm^{-2}) every five cycles. Ex situ XRD measurements were performed at five states: before cycling, after the first charge, after the first discharge, after the second charge, and after the second discharge. X-ray photoelectron spectroscopy (XPS; K-Alpha, ULVAC-PHI, Inc.) was conducted at the same states.

All sample handling and cell assembly procedures were performed at 30 °C in a dry Ar atmosphere.

■ ASSOCIATED CONTENT

Data Availability Statement

Data supporting this study are available from the corresponding author upon reasonable request.

Supporting Information

The Supporting Information is available free of charge at https://pubs.acs.org/doi/10.1021/acsmaterialslett.6c00297.

Details of machine-learning-based synthesizability screening; calculation methods for stack-level energy density; computational methods for density functional theory and Crystal Orbital Hamilton Population analyses; tables of predicted synthetic accessibility, interatomic distances, distribution of relaxation times parameters, X-ray photoelectron spectroscopy elemental quantification, and cell design parameters; supplementary figures showing reference crystal structures, reverse Monte Carlo structural models, DC polarization, scanning electron microscopy images, Arrhenius plots, quantitative ruthenium oxidation states, projected density of states, Nyquist plots, and rate performance evaluations (DOCX)

■ AUTHOR INFORMATION

Corresponding Author

Naoto Tanibata – *Department of Advanced Ceramics, Nagoya Institute of Technology, Nagoya, Aichi 466-8555, Japan;* orcid.org/0000-0001-8521-9690; Email: tanibata.naoto@nitech.ac.jp

Authors

Shin Aizu – *Department of Advanced Ceramics, Nagoya Institute of Technology, Nagoya, Aichi 466-8555, Japan*

Takuhiro Sasadaira – *Department of Advanced Ceramics, Nagoya Institute of Technology, Nagoya, Aichi 466-8555, Japan*

Hayami Takeda – *Department of Advanced Ceramics, Nagoya Institute of Technology, Nagoya, Aichi 466-8555, Japan;* orcid.org/0000-0001-9499-9684

Masanobu Nakayama – *Department of Advanced Ceramics, Nagoya Institute of Technology, Nagoya, Aichi 466-8555, Japan;* orcid.org/0000-0002-5113-053X

Koji Ohara – *Faculty of Materials for Energy, Shimane University, Matsue, Shimane 690-8504, Japan*; orcid.org/0000-0002-3134-512X

Complete contact information is available at: https://pubs.acs.org/doi/10.1021/acsmaterialslett.6c00297

Author Contributions

Conceptualization: N.T. Formal analysis: N.T. and K.O. Funding acquisition: N.T. and M.N. Investigation: S.A. Project administration: N.T. and M.N. Resources: N.T. and M.N. Supervision: N.T. and M.N. Validation: T.S. Visualization: S.A. and T.S. Writing—original draft: S.A. and N.T. Writing—review & editing: H.T., M.N., and K.O.

Notes

The authors declare no competing financial interest.

■ ACKNOWLEDGEMENTS

This study was partially supported by Grants-in-Aid for Scientific Research (grant numbers 24K01157, 24K17755, 24H02203, 25H01979, and 25H01973) from the Ministry of Education, Culture, Sports, Science, and Technology (MEXT), Japan, a CREST grant from the Japan Science and Technology Agency, Japan (grant number JPMJCR21O6), the Data Creation and Utilization-Type Material Research and Development Project (grant number JPMXP1122712807) from MEXT and a grant from the Electrochemical Society of Japan (grant number KF017206). The synchrotron radiation experiments were performed at BL04B2 of SPring-8 with the approval of the Japan Synchrotron Radiation Research Institute (Proposal No. 2024B1026).

■ REFERENCES

(1) Dunn, B.; Kamath, H.; Tarascon, J. M. Electrical Energy Storage for the Grid: A Battery of Choices. *Science* **2011**, 928−935 .

(2) Janek, J.; Zeier, W. G. A Solid Future for Battery Development *Nat. Energy* **2016**, *1*, 16141.

(3) Li, J.; Ma, C.; Chi, M.; Liang, C.; Dudney, N. J. Solid Electrolyte: The Key for High-Voltage Lithium Batteries. *Adv. Energy Mater.* **2015**, *5*, 1401408.

(4) Yan, Y.; Zhang, S.; Li, Q.; Man, X.; Jiang, X.; Xiong, S.; Mi, C.; Zhang, Z.; Wang, C.; Xiao, P.; Yin, L.; Wang, R. Versatile Polymer-Supported Argyrodite-Type Sulfide Solid Electrolyte Membranes for Energy-Dense Lithium Batteries. *Mater. Sci. Eng., R* **2025**, *163*, 100941.

(5) Goodenough, J. B.; Kim, Y. Challenges for Rechargeable Li Batteries. *Chem. Mater.* **2010**, *22*, 587−603.

(6) Tanibata, N.; Nonaka, N.; Urushihara, D.; Takeda, H.; Kobayashi, R.; Kuwata, N.; Nakayama, M. High-Throughput Screening and Characterization of Non-Flammable Na-Cl Solid Electrolytes. *Adv. Electron. Mater.* **2026**, *12*, e00688.

(7) Fang, R.; Zhao, S.; Sun, Z.; Wang, D. W.; Cheng, H. M.; Li, F. More Reliable Lithium-Sulfur Batteries: Status, Solutions and Prospects. *Adv. Mater.* **2017**, *9*, 1606823.

(8) Tanibata, N.; Tsukasaki, H.; Deguchi, M.; Mori, S.; Hayashi, A.; Tatsumisago, M. A Novel Discharge-Charge Mechanism of a S-P2S5 Composite Electrode without Electrolytes in All-Solid-State Li/S Batteries. *J. Mater. Chem. A* **2017**, *5*, 11224−11228.

(9) Wang, K.; Gu, Z.; Xi, Z.; Hu, L.; Ma, C. Li_3TiCl_6 as Ionic Conductive and Compressible Positive Electrode Active Material for All-Solid-State Lithium-Based Batteries. *Nat. Commun.* **2023**, *14*, 1396.

(10) Liu, Z.; Liu, J.; Zhao, S.; Xun, S.; Byaruhanga, P.; Chen, S.; Tang, Y.; Zhu, T.; Chen, H. Low-Cost Iron Trichloride Cathode for All-Solid-State Lithium-Ion Batteries. *Nat. Sustainability* **2024**, *7*, 1492−1500.

(11) Tanibata, N.; Takimoto, S.; Aizu, S.; Takeda, H.; Nakayama, M. Applying the HSAB Design Principle to the 3.5 V-Class All-Solid-State Li-Ion Batteries with a Chloride Electrolyte. *J. Mater. Chem. A* **2022**, *10*, 20756−20760.

(12) Mulliken, R. S. A New Electroaffinity Scale; Together with Data on Valence States and on Valence Ionization Potentials and Electron Affinities. *J. Chem. Phys.* **1934**, *2*, 782−793.

(13) Tanibata, N.; Kato, M.; Takimoto, S.; Takeda, H.; Nakayama, M.; Sumi, H. High Formability and Fast Lithium Diffusivity in Metastable Spinel Chloride for Rechargeable All-solid-state Lithium-ion Batteries. *Adv. Energy Sustainability Res.* **2020**, *1*, 2000025.

(14) Kitaura, H.; Takahashi, K.; Mizuno, F.; Hayashi, A.; Tadanaga, K.; Tatsumisago, M. Preparation of α-Fe[Sub 2]O[Sub 3] Electrode Materials via Solution Process and Their Electrochemical Properties in All-Solid-State Lithium Batteries. *J. Electrochem. Soc.* **2007**, *154*, A725−A729.

(15) Brec, R.; Dugast, A.; Le Mehauté, A. Chemical and electrochemical study of the Li_xFeS_2 cathodic system ($0 < x < 2$). *Mater. Res. Bull.* **1980**, *15*, 619−625.

(16) Sakuda, A.; Kitaura, H.; Hayashi, A.; Tatsumisago, M.; Hosoda, Y.; Nagakane, T.; Sakamoto, A. All-Solid-State Lithium Secondary Batteries Using $Li_2SP_2S_5$ Solid Electrolytes and $LiFePO_4$ Electrode Particles with Amorphous Surface Layer. *Chem. Lett.* **2012**, *41*, 260−261.

(17) Kim, J. Y.; Park, J.; Kang, S. H.; Jung, S.; Shin, D. O.; Lee, M. J.; Oh, J.; Kim, K. M.; Zausch, J.; Lee, Y. G.; Lee, Y. M. Revisiting TiS_2 as a Diffusion-Dependent Cathode with Promising Energy Density for All-Solid-State Lithium Secondary Batteries. *Energy Storage Mater.* **2021**, *41*, 289−296.

(18) Liang, J.; Li, X.; Kim, J. T.; Hao, X.; Duan, H.; Li, R.; Sun, X. Halide Layer Cathodes for Compatible and Fast-Charged Halides-Based All-Solid-State Li Metal Batteries. *Angew. Chem.* **2023**, *135*, e202217081.

(19) Tanibata, N.; Aizu, S.; Sasadaira, T.; Takeda, H.; Nakayama, M. Redox-Level Design for High-Energy-Density Chloride Electrodes. *Adv. Energy Mater.* **2025**, *15*, e04110.

(20) Ishiguro, Y.; Ueno, K.; Nishimura, S.; Iida, G.; Igarashib, Y. $TaCl_5$ -Glassified Ultrafast Lithium Ion-Conductive Halide Electrolytes for High-Performance All-Solid-State Lithium Batteries. *Chem. Lett.* **2023**, *52*, 237−241.

(21) Kadono, K. Nonoxide Glass-Forming Systems - Glass Formation and Structure, and Optical Properties of Rare-Earth Ions in Glasses. *J. Ceram. Soc. Jpn.* **2007**, *115*, 297−303.

(22) Zhang, S.; Zhao, F.; Chen, J.; Fu, J.; Luo, J.; Alahakoon, S. H.; Chang, L. Y.; Feng, R.; Shakouri, M.; Liang, J.; Zhao, Y.; Li, X.; He, L.; Huang, Y.; Sham, T. K.; Sun, X. A Family of Oxychloride Amorphous Solid Electrolytes for Long-Cycling All-Solid-State Lithium Batteries. *Nat. Commun.* **2023**, *14*, 3780.

(23) Yan, Y.; Zhang, S.; Man, X.; Li, Q.; Xue, H.; Xiao, P.; Shi, Y.; Yin, L.; Wang, R. Emerging Inorganic Amorphous Solid-State Electrolytes in All-Solid-State Lithium Batteries: From Crystallographic Order to Atomic and Lattice Disorder. *eScience* **2026**, *6*, 100531.

(24) Aizu, S.; Takimoto, S.; Tanibata, N.; Takeda, H.; Nakayama, M.; Kobayashi, R. Screening Chloride Li-Ion Conductors Using High-Throughput Force-Field Molecular Dynamics. *J. Am. Ceram. Soc.* **2023**, *106*, 3035−3044.

(25) Tanibata, N.; Aizu, S.; Koga, M.; Takeda, H.; Kobayashi, R.; Nakayama, M. Guidelines for Designing High-Deformability Materials for All-Solid-State Lithium-Ion Batteries. *J. Mater. Chem. A* **2024**, *12*, 15601−15607.

(26) Jain, A.; Ong, S. P.; Hautier, G.; Chen, W.; Richards, W. D.; Dacek, S.; Cholia, S.; Gunter, D.; Skinner, D.; Ceder, G.; Persson, K. A. Commentary: The Materials Project: A Materials Genome Approach to Accelerating Materials Innovation *APL Mater.* **2013**, *1*, 011002.

(27) Atsumi, T.; Sato, K.; Yamaguchi, Y.; Hamaie, M.; Yasuda, R.; Tanibata, N.; Takeda, H.; Nakayama, M.; Karasuyama, M.; Takeuchi, I. Chemical Composition Data-Driven Machine-Learning Prediction for Phase Stability and Materials Properties of Inorganic Crystalline Solids. *Phys. Status Solidi B* **2022**, *259*, 2100525.

(28) Wu, Y.; Zhou, K.; Ren, F.; Ha, Y.; Liang, Z.; Zheng, X.; Wang, Z.; Yang, W.; Zhang, M.; Luo, M.; Battaglia, C.; Yang, W.; Zhu, L.; Gong, Z.; Yang, Y. Highly Reversible Li $_2$ RuO $_3$ Cathodes in Sulfide-Based All Solid-State Lithium Batteries. *Energy Environ. Sci.* **2022**, *15*, 3470−3482.

(29) Lin, R.; Hu, E.; Liu, M.; Wang, Y.; Cheng, H.; Wu, J.; Zheng, J.-C.; Wu, Q.; Bak, S.; Tong, X.; Zhang, R.; Yang, W.; Persson, K. A.; Yu, X.; Yang, X.-Q.; Xin, H. L. Anomalous Metal Segregation in Lithium-Rich Material Provides Design Rules for Stable Cathode in Lithium-Ion Battery. *Nat. Commun.* **2019**, *10*, 1650.

(30) Li, H.; Ramakrishnan, S.; Freeland, J. W.; McCloskey, B. D.; Cabana, J. Definition of Redox Centers in Reactions of Lithium Intercalation in Li_3RuO_4 Polymorphs. *J. Am. Chem. Soc.* **2020**, *142*, 8160−8173.

(31) Margoutidis, G.; Parsons, V. H.; Bottaro, C. S.; Yan, N.; Kerton, F. M. Mechanochemical Amorphization of α-Chitin and Conversion into Oligomers of N-Acetyl-D-Glucosamine. *ACS Sustainable Chem. Eng.* **2018**, *6*, 1662−1669.

(32) Tang, K.; Yu, X.; Sun, J.; Li, H.; Huang, X. Kinetic Analysis on $LiFePO_4$ Thin Films by CV, GITT, and EIS. *Electrochim. Acta* **2011**, *56*, 4869−4875.

(33) Kuwata, N.; Nakane, M.; Miyazaki, T.; Mitsuishi, K.; Kawamura, J. Lithium Diffusion Coefficient in $LiMn_2O_4$ Thin Films Measured by Secondary Ion Mass Spectrometry with Ion-Exchange Method. *Solid State Ionics* **2018**, *320*, 266−271.

(34) Sayed, F. N.; Sreedhara, M. B.; Soni, A.; Bhat, U.; Datta, R.; Bhattacharyya, A. J.; Rao, C. N. R. Li and Na-Ion Diffusion and Intercalation Characteristics in Vertically Aligned TiS_2 Nanowall Network Grown Using Atomic Layer Deposition. *Mater. Res. Express* **2019**, *6*, 115549.

(35) Imanishi, N.; Kanamura, K.; Takehara, Z. I. Synthesis of Mos_2 Thin Film by Chemical Vapor Deposition Method and Discharge Characteristics as a Cathode of the Lithium Secondary Battery. *J. Electrochem. Soc.* **1992**, *139*, 2082−2087.

(36) Sasadaira, T.; Tanibata, N.; Takeda, H.; Nakayama, M. Enhanced Li-Ion Conductivity of Li_2 $FeCl_4$ Cathode Material by Partial Br Substitution. *J. Asian Ceram. Soc.* **2026**, *14*, 79−86.

(37) Maier, J. Mass Transport in the Presence of Internal Defect Reactions—Concept of Conservative Ensembles: IV, Tracer Diffusion and Intercorrelation with Chemical Diffusion and Ion Conductivity. *J. Am. Ceram. Soc.* **1993**, *76*, 1228−1232.

(38) Van der Ven, A.; Ceder, G.; Asta, M.; Tepesch, P. D. First-Principles Theory of Ionic Diffusion with Nondilute Carriers. *Phys. Rev. B* **2001**, *64*, 184307.

(39) Malkow, K. T. A Theory of Distribution Functions of Relaxation Times for the Deconvolution of Immittance Data. *J. Electroanal. Chem.* **2019**, *838*, 221−231.

(40) Irvine, J. T. S.; Sinclair, D. C.; West, A. R. Electroceramics: Characterization by Impedance Spectroscopy. *Adv. Mater.* **1990**, 132−138.

(41) Zhang, S.; Fang, S.; Chen, J.; Ni, L.; Deng, W.; Zou, G.; Hou, H.; Ji, X. Engineering D-p Orbital Hybridization for High-Stable Lithium Manganate Cathode. *Chem. Eng. J.* **2023**, *451*, 138511.

(42) Wang, T.; Ren, G. X.; Xia, H. Y.; Shadike, Z.; Huang, T. Q.; Li, X. L.; Yang, S. Y.; Chen, M. W.; Liu, P.; Gao, S. P.; Liu, X. S.; Fu, Z. W. Anionic Redox Regulated via Metal−Ligand Combinations in Layered Sulfides. *Adv. Mater.* **2021**, *34*, 2107353.

(43) Dronskowski, R.; Bloechl, P. E. Crystal Orbital Hamilton Populations (COHP): Energy-Resolved Visualization of Chemical Bonding in Solids Based on Density-Functional Calculations. *J. Phys. Chem.* **1993**, *97*, 8617−8624.

(44) Hakari, T.; Fujita, Y.; Deguchi, M.; Kawasaki, Y.; Otoyama, M.; Yoneda, Y.; Sakuda, A.; Tatsumisago, M.; Hayashi, A. Solid Electrolyte with Oxidation Tolerance Provides a High-Capacity Li_2S-Based Positive Electrode for All-Solid-State Li/S Batteries *Adv. Funct. Mater.* **2022**, *32*, 2106174.

(45) Tanibata, N.; Kondo, S.; Akatsuka, S.; Takeda, H.; Nakayama, M. Fast Anion Redox by Amorphization in Sodium-Ion Batteries. *Chem. Mater.* **2025**, *37*, 303−312.

(46) Zhang, W.; Richter, F. H.; Culver, S. P.; Leichtweiss, T.; Lozano, J. G.; Dietrich, C.; Bruce, P. G.; Zeier, W. G.; Rgen Janek, J. Degradation Mechanisms at the $Li_{10}GeP_2S_{12}/LiCoO_2$ Cathode Interface in an All-Solid-State Lithium-Ion Battery. **2018**, *10*, 22226–22236.

(47) Auvergniot, J.; Cassel, A.; Ledeuil, J.-B.; Viallet, V.; Seznec, V.; Dedryve, R. Interface Stability of Argyrodite Li_6PS_5Cl toward $LiCoO_2$, $LiNi_{1/3}Co_{1/3}Mn_{1/3}O_2$, and $LiMn_2O_4$ in Bulk All-Solid-State Batteries. *Chem. Mater.* **2017**, *29*, 3883–3890.

(48) Asano, T.; Sakai, A.; Ouchi, S.; Sakaida, M.; Miyazaki, A.; Hasegawa, S. Solid Halide Electrolytes with High Lithium-Ion Conductivity for Application in 4 V Class Bulk-Type All-Solid-State Batteries. *Adv. Mater.* **2018**, *30*, 1803075.

(49) Li, X.; Liang, J.; Chen, N.; Luo, J.; Adair, K. R.; Wang, C.; Banis, M. N.; Sham, T. K.; Zhang, L.; Zhao, S.; Lu, S.; Huang, H.; Li, R.; Sun, X. Water-Mediated Synthesis of a Superionic Halide Solid Electrolyte. *Angew. Chem., Int. Ed.* **2019**, *58*, 16427−16432.

(50) Park, K. H.; Kaup, K.; Assoud, A.; Zhang, Q.; Wu, X.; Nazar, L. F. High-Voltage Superionic Halide Solid Electrolytes for All-Solid-State Li-Ion Batteries *ACS Energy Lett.* **2020**, *5*, 533−539.

(51) Liang, J.; Li, X.; Wang, S.; Adair, K. R.; Li, W.; Zhao, Y.; Wang, C.; Hu, Y.; Zhang, L.; Zhao, S.; Lu, S.; Huang, H.; Li, R.; Mo, Y.; Sun, X. Site-Occupation-Tuned Superionic Li_xScCl^{3+} XHalide Solid Electrolytes for All-Solid-State Batteries. *J. Am. Chem. Soc.* **2020**, *142*, 7012−7022.

(52) Kwak, H.; Han, D.; Lyoo, J.; Park, J.; Jung, S. H.; Han, Y.; Kwon, G.; Kim, H.; Hong, S. T.; Nam, K. W.; Jung, Y. S. New Cost-Effective Halide Solid Electrolytes for All-Solid-State Batteries: Mechanochemically Prepared Fe^{3+}-Substituted Li_2ZrCl_6. *Adv. Energy Mater.* **2021**, *11*, 2003190.

(53) Yu, Y.; Wang, Z.; Shao, G. Formulation of Li-Metal-Halide (LMX) Solid State Electrolytes through Extensive First Principles Modelling. *J. Mater. Chem. A* **2021**, *9*, 25585−25594.

(54) Kwak, H.; Kim, J. S.; Han, D.; Kim, J. S.; Park, J.; Kwon, G.; Bak, S. M.; Heo, U.; Park, C.; Lee, H. W.; Nam, K. W.; Seo, D. H.; Jung, Y. S. Boosting the Interfacial Superionic Conduction of Halide Solid Electrolytes for All-Solid-State Batteries *Nat. Commun.* **2023**, *14*:1, 2459.

(55) Yan, X.; Li, Z.; Wen, Z.; Han, W. $Li/Li_7La_3Zr_2O_{12}/LiFePO_4$ All-Solid-State Battery with Ultrathin Nanoscale Solid Electrolyte. *J. Phys. Chem. C* **2017**, *121*, 1431−1435.

(56) Cronk, A.; Chen, Y. T.; Deysher, G.; Ham, S. Y.; Yang, H.; Ridley, P.; Sayahpour, B.; Nguyen, L. H. B.; Oh, J. A. S.; Jang, J.; Tan, D. H. S.; Meng, Y. S. Overcoming the Interfacial Challenges of $LiFePO_4$ in Inorganic All-Solid-State Batteries. *ACS Energy Lett.* **2023**, *8*, 827−835.

(57) Kitaura, H.; Hayashi, A.; Tadanaga, K.; Tatsumisago, M. Improvement of Electrochemical Performance of All-Solid-State Lithium Secondary Batteries by Surface Modification of $LiMn_2O_4$ Positive Electrode. *Solid State Ionics* **2011**, *192*, 160−163.

(58) Ohara, K.; Tominaka, S.; Yamada, H.; Takahashi, M.; Yamaguchi, H.; Utsuno, F.; Umeki, T.; Yao, A.; Nakada, K.; Takemoto, M.; Hiroi, S.; Tsuji, N.; Wakihara, T. Time-Resolved Pair Distribution Function Analysis of Disordered Materials on Beamlines BL04B2 and BL08W at SPring-8. *J. Synchrotron Radiat.* **2018**, *25*, 1627−1633.

(59) Gereben, O.; Jóvári, P.; Temleitner, L.; Pusztai, L. A New Version of the RMC++ Reverse Monte Carlo Programme, Aimed at Investigating the Structure of Covalent Glasses. *J. Optoelectron. Adv. Mater.* **2007**, *9*, 3021−2027.

(60) Takamoto, S.; Shinagawa, C.; Motoki, D.; Nakago, K.; Li, W.; Kurata, I.; Watanabe, T.; Yayama, Y.; Iriguchi, H.; Asano, Y.; Onodera, T.; Ishii, T.; Kudo, T.; Ono, H.; Sawada, R.; Ishitani, R.; Ong, M.; Yamaguchi, T.; Kataoka, T.; Hayashi, A.; Charoenphakdee, N.;

https://doi.org/10.1021/acsmaterialslett.6c00297
ACS Mater. Lett. XXXX, XXX, XXX–XXX

Ibuka, T. Towards Universal Neural Network Potential for Material Discovery Applicable to Arbitrary Combination of 45 Elements. *Nat. Commun.* **2022**, *13*, 2991.

(61) Sumi, H.; Shimada, H.; Yamaguchi, Y.; Yamaguchi, T.; Fujishiro, Y. Degradation Evaluation by Distribution of Relaxation Times Analysis for Microtubular Solid Oxide Fuel Cells. *Electrochim. Acta* **2020**, *339*, 135913.

(62) Santhosha, A. L.; Medenbach, L.; Buchheim, J. R.; Adelhelm, P. The Indium−Lithium Electrode in Solid-State Lithium-Ion Batteries: Phase Formation, Redox Potentials, and Interface Stability. *Batteries Supercaps* **2019**, *2*, 524−529.

https://doi.org/10.1021/acsmaterialslett.6c00297
ACS Mater. Lett. XXXX, XXX, XXX−XXX